Microscale mechanical properties in sintered copper nanoparticles

Yan, Xuyang; Du, Leiming; Gu, Chao; Tian, Tiancheng; Gao, Chenshan; Zhang, Guoqi; Fan, Jiajie

DOI
10.1016/j.msea.2025.148684

Publication date
2025

Document Version
Final published version

Published in
Materials Science and Engineering: A

Materials Science & Engineering A 943 (2025) 148684

Contents lists available at ScienceDirect

Materials Science & Engineering A

journal homepage: www.elsevier.com/locate/msea

Microscale mechanical properties in sintered copper nanoparticles

Xuyang Yan [a], Leiming Du [b,*], Chao Gu [a], Tiancheng Tian [a,c], Chenshan Gao [d], Guoqi Zhang [b], Jiajie Fan [a,b,e,**]

[a] Shanghai Engineering Technology Research Center of SiC Power Device, College of Intelligent Robotics and Advanced Manufacturing, Fudan University, 220 Handan Rd., Shanghai, 200433, China
[b] Department of Microelectronics, Delft University of Technology, Mekelweg 4, Delft, 2628 CD, The Netherlands
[c] Boschman Advanced Packaging Technology, 188 Zixu Rd., Suzhou, 215164, China
[d] School of Microelectronics, Southern University of Science and Technology, Nanshan i Park Chongwen, Shenzhen, 518055, China
[e] Research Institute of Fudan University in Ningbo, 901 Binhai Second Rd., Ningbo, 315336, China

ARTICLE INFO

Keywords:
Sintering cu nanoparticles
In-situ micro-pillar compression test
Transmission Kikuchi diffraction
Size effect
Molecular dynamics simulation

ABSTRACT

This study investigates the size-dependent mechanical behavior and deformation mechanisms of sintered copper (Cu) nanoparticles (NPs) through micro-pillar (2–6 μm diameter) compression tests, scanning electron microscopy (SEM), transmission electron microscopy (TEM), transmission Kikuchi diffraction (TKD) analysis and molecular dynamics (MD) simulations. In-situ micro-pillar compression tests reveal a 25.9% reduction in yield strength (812 ± 64 MPa to 643 ± 47 MPa) with increasing pillar size, attributed to dislocation starvation in smaller pillars and porosity-driven strain localization in larger ones. TKD quantifies dynamic grain refinement (24.9% reduction in grain size) and geometrically necessary dislocation (GND) density escalation (74.8%), driven by stress gradients and grain boundary-mediated plasticity. Nanoindentation-derived elastic modulus (48.3 ± 11.1 GPa) exceeds micropillar values (29.5–33.9 GPa), reflecting substrate constraints in bulk testing. Microstructural analysis identifies a transition from shear banding in high-porosity pillars to uniform plasticity in denser systems, mediated by texture evolution (Brass/S components) and Schmid factor redistribution (62% increase in high-slip-activity grains). MD simulations of pressure-sintered Cu NPs elucidate atomic-scale mechanisms: dislocation nucleation at sintering necks, pore collapse-induced strain localization, and grain boundary sliding. These findings establish a multiscale framework linking porosity, grain refinement, and dislocation dynamics to mechanical performance, emphasizing microstructural optimization for enhanced reliability in microelectronic applications. The integration of MD simulations bridges atomic-scale mechanisms to microscale deformation, providing actionable insights for tailoring sintered Cu NPs via reduced porosity and controlled grain boundary architectures.

1. Introduction

Metallic nanoparticles (NPs), such as copper (Cu) and silver (Ag), exhibit unique low-temperature sintering behavior due to their high surface energy [1]. This property promotes the formation of thermodynamically stable structures while maintaining functional performance even under elevated thermal conditions [2,3]. Among these materials, sintered Cu NPs offer distinct advantages, including cost-effectiveness and excellent resistance to electromigration [4], surpassing the performance of Ag NPs in these aspects. These attributes make Cu NPs highly suitable for advanced applications in power electronics packaging, where both thermal and electrical reliability are critical. Despite their operational benefits, the mechanical properties of sintered Cu nanoparticle (NP) structures, particularly at the microscale, remain insufficiently characterized. Addressing this gap in knowledge is essential for optimizing material design and enabling the effective deployment of Cu NP-based technologies in high-performance electronic systems.

Many previous studies have predominantly relied on conventional mechanical testing methodologies, such as shear tests and tensile tests [5–7], to evaluate the properties of sintered materials. However, these macroscale approaches are inherently limited in their ability to capture the intrinsic mechanical behavior of sintered systems, particularly for nanostructured materials like Cu NPs. A fundamental challenge stems from the dimensional mismatch between standardized bulk test specimens and the microscale operational dimensions (typically tens

* Corresponding author.
** Corresponding author at: Shanghai Engineering Technology Research Center of SiC Power Device, College of Intelligent Robotics and Advanced Manufacturing, Fudan University, 220 Handan Rd., Shanghai, 200433, China.
E-mail addresses: L.Du@tudelft.nl (L. Du), jiajie_fan@fudan.edu.cn (J. Fan).

https://doi.org/10.1016/j.msea.2025.148684
Received 30 May 2025; Accepted 16 June 2025
Available online 14 July 2025

of micrometers) in practical applications [8], where size-dependent phenomena and scaling effects distort the extrapolation of bulk-derived data to service-relevant conditions. While microscale techniques such as nanoindentation have been employed to probe localized mechanical responses in sintered Cu NPs, this method remains insufficient for resolving spatially heterogeneous deformation mechanisms or correlating microstructure with sub-micron mechanical behavior [9]. In contrast, micro-pillar compression experiments conducted under scanning electron microscopy (SEM) enable in situ quantification of mechanical properties at application-relevant scales [10–16]. This integrated approach provides a robust framework for elucidating deformation pathways, failure modes, and structure–property relationships in complex sintered systems [13,17,18], thereby addressing critical gaps in predicting the reliability of Cu NP-based structures under operational stresses.

Micro-pillar compression studies of bulk crystalline metals have demonstrated significant size-dependent mechanical behavior [19–21], where face-centered cubic (FCC) single crystals exhibit power-law strengthening with decreasing pillar diameter due to dislocation starvation mechanisms [22,23]. As pillar dimensions reduce, dislocations are expelled from free surfaces faster than they nucleate, leading to reduced dislocation density and requiring higher stresses to activate new sources—a phenomenon experimentally validated in Ni single crystals [24,25]. Conversely, nanocrystalline systems display inverse size effects; for example, sub-100 nm Ni-W pillars exhibit strength degradation as deformation transitions from dislocation-mediated plasticity to grain boundary-dominated mechanisms [26].

In sintered NP systems, porosity introduces distinct challenges by acting as stress concentrators that degrade mechanical properties and promote strain localization [27–30]. While prior work has characterized porosity effects in sintered Ag NPs [16], the mechanical behavior of sintered Cu NPs—particularly at microscale service dimensions—remains poorly understood. The interplay between intrinsic size effects (e.g., dislocation starvation) and extrinsic porosity-driven mechanisms (e.g., void coalescence) in Cu NPs is unresolved, as their unique sintering dynamics (e.g., necking geometry) may alter deformation pathways. This gap underscores the need to investigate sintered Cu NPs under operational conditions, where novel failure mechanisms—such as synergistic dislocation–porosity interactions—are anticipated to govern their structural integrity.

The experimental characterization of submicron-scale deformation mechanisms in sintered NPs remains constrained by challenges in fabricating hierarchical microstructures and resolving localized plasticity. Consequently, computational methods such as molecular dynamics (MD) [31–33], discrete dislocation dynamics (DDD) [34,35], and crystal plasticity finite element modeling (CPFEM) [36,37] have emerged as critical tools for probing dislocation-mediated mechanisms. DDD, grounded in dislocation elasticity theory, enables direct simulation of dislocation microstructure evolution under deformation [38], while CPFEM captures heterogeneous mechanical behavior, including plastic strain localization, texture evolution, and dislocation density dynamics at mesoscopic scales [39,40]. For instance, Long et al. [40] employed CPFEM to correlate the mesostructural evolution of sintered Ag NPs—specifically grain size and initial orientation—with macroscopic mechanical degradation. MD simulations, though limited by temporal and spatial constraints, have provided atomistic insights into NP sintering processes, including neck formation and stress-assisted densification via plastic flow [41,42]. However, prior MD studies predominantly utilized simplified models with fewer than tens of particles [43,44], inadequately representing the anisotropic microstructures observed in pressure-sintered Cu NPs [33]. Recent advances propose stochastic particle distribution models that better replicate the microstructure of sintered Cu NPs [33]. These integrated approaches synergistically elucidate dislocation-void interplay and strain localization mechanisms, resolving critical knowledge gaps in the micromechanical response of sintered Cu NP aggregates.

In this work, an integrated experimental–computational approach is employed to investigate the size-dependent mechanical behavior of sintered Cu NP micro-pillars. Micro-pillars with diameters of 2, 4 and 6 μm were fabricated via focused ion beam (FIB) milling and subjected to in situ uniaxial compression testing inside a SEM to obtain stress–strain responses. Complementary nanoindentation tests using a spherical indenter were conducted to assess bulk-scale mechanical properties. Post-deformation microstructural analysis was performed using transmission electron microscopy (TEM) and transmission Kikuchi diffraction (TKD) to reveal deformation mechanisms and grain orientation evolution. Additionally, MD simulations were carried out to capture atomic-scale phenomena, including dislocation activity, porosity interactions, and strain localization during compression. This comprehensive study establishes a direct correlation between microstructural features and mechanical performance, highlighting the influence of pillar size and porosity on the deformation behavior of sintered Cu NPs.

2. Material preparation and test methods

2.1. Sintered Cu NPs preparation

Fig. 1 illustrates the preparation protocol for pressure-assisted sintered Cu NP specimens. A Cu NP slurry, synthesized via a method adapted from prior methodology [29], was uniformly deposited onto an active metal brazed (AMB) substrate using screen printing to achieve a 100 μm-thick layer. The printed specimen was thermally treated under a nitrogen environment at 120 °C for 5 min to remove solvents. A 5 mm × 5 mm silicon carbide (SiC) chip was then precisely aligned and bonded to the dried Cu NP layer using an automated die-attach system. Sintering was performed under a nitrogen atmosphere at 250 °C with an applied uniaxial pressure of 20 MPa for 3 min to ensure interfacial densification. Post-sintering, cross-sectional specimens were prepared by sectioning the sintered assembly along the chip centerline using a diamond saw. These sections were cold-mounted in epoxy resin to preserve structural integrity during subsequent metallographic preparation. Final polishing with progressively refined abrasives yielded a deformation-free surface, enabling high-resolution microstructural characterization and focused ion beam (FIB) milling of micro-pillars for mechanical testing.

2.2. Micro-pillar compression and nanoindentation tests

Micro-pillar arrays with diameters of 2, 4, and 6 μm were fabricated on sintered Cu NP specimens using a focused ion beam-scanning electron microscope (FIB-SEM, Thermo Scientific Helios 5 DualBeam) operated at 30 kV. Five pillars per size were milled to study size-dependent mechanical behavior (Fig. 2). Initial coarse milling utilized a high-current Ga^+ ion beam (9 nA to 2.1 nA) to isolate pillars, followed by low-current polishing (20 pA) to finalize geometries, minimize surface defects, and mitigate FIB-induced hardening. Pillar dimensions were verified via SEM to ensure an aspect ratio of 2.5, balancing buckling resistance and end-face artifact avoidance [45].

Uniaxial compression tests were performed in situ using a nanoindentation system integrated with the SEM (Fig. 2a). A high-sensitivity load cell and precision encoder captured force–displacement data at sub-nanometer resolution under displacement control. Strain rates were maintained at 0.006 s^{-1} across all pillars by adjusting displacement rates proportionally to pillar diameter (30–90 nm/s; Table S1). Flat diamond punches (6 μm for 2–4 μm pillars; 10 μm for 6 μm pillars) were aligned via high-resolution SEM to ensure axial loading and uniform stress distribution (Fig. 2b), minimizing contact zone artifacts. Tests concluded at 60% engineering strain or upon observable failure (e.g., buckling, cracking).

Nanoindentation tests were performed on the sintered specimens using a G200 nanoindenter (Keysight, USA) equipped with a spherical diamond tip (Synton MPD, Nidau, Switzerland) and the continuous

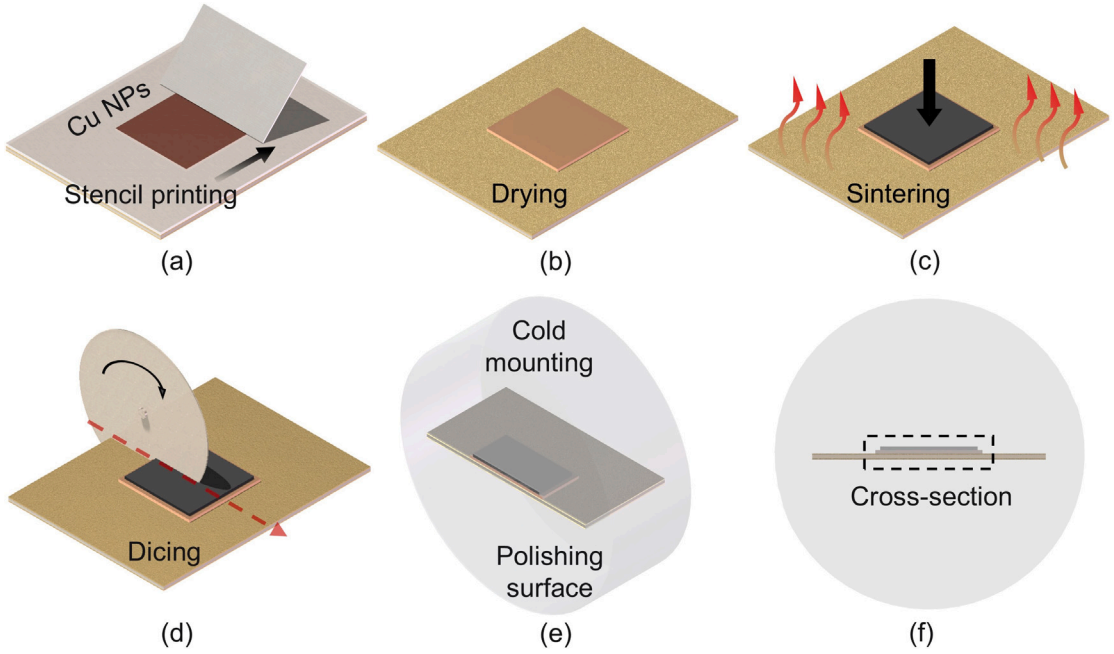

Fig. 1. Preparation process of pressure-assisted sintered Cu samples: (a) Screen printing; (b) drying; (c) sintering (250 °C, 20 MPa, 3 min); (d) sectioning; (e) metallographic cold mounting; (f) polishing.

stiffness measurement (CSM) module. The spherical tip, preferred over the conventional Berkovich tip for probing nanoporous structures, provides a more uniform stress distribution and mitigates stress concentration effects, enabling more reliable assessment of mechanical properties [46]. Prior to testing, the tip area function was carefully calibrated. Indentations were carried out in strain rate-controlled mode with a constant indentation strain rate of 0.05 s^{-1}, up to a maximum penetration depth of 2.5 μm. Four indentations were performed on each sample with 100 μm spacing to ensure statistical consistency.

2.3. TEM and TKD characterization

Microstructural evolution in sintered Cu NP micro-pillars was investigated using a correlative approach combining TEM and TKD, conducted on a Zeiss GeminiSEM 360 and a Hitachi Regulus 8230, respectively. TEM imaging enabled direct observation of localized dislocation activity, strain gradients, and nanoscale features such as sintering necks and internal stacking faults, particularly after compression. As shown in Fig. 3, the as-sintered microstructure exhibits a porous morphology with interconnected particles and well-defined sintering necks. To complement these observations, TKD provided high-resolution grain orientation maps and insights into grain boundary network evolution, offering a quantitative basis for understanding crystallographic anisotropy and its relation to size-dependent mechanical behavior. While electron backscatter diffraction (EBSD) is commonly employed in micromechanical studies to assess crystallographic changes [47–49], its limited spatial resolution (50-100 nm) renders it inadequate for characterizing the submicron grain structure and porosity of sintered Cu NP pillars. TKD overcomes this constraint by achieving spatial resolutions below 10 nm [50,51], thus enabling statistically robust microstructural characterization essential for interpreting deformation mechanisms at the microscale.

Axial longitudinal cross-sections of compressed 6 μm micro-pillars were extracted via FIB milling to preserve deformation gradients inherent to the sintered Cu NP microstructure. The sections were thinned to sub-50 nm thickness to optimize TKD signal resolution while minimizing electron beam-induced artifacts. Crystallographic orientation maps and grain boundary misorientation distributions were generated using EDAX OIM Analysis software, with Schmid factor analysis applied to quantify slip system activation and crystallographic anisotropy.

2.4. Molecular dynamics simulation

Molecular dynamics (MD) simulations of Cu NPs sintering and mechanical behavior were conducted using the Large-scale Atomic/Molecular Massively Parallel Simulator (LAMMPS) [52], with atomic interactions modeled via the Mishin embedded atom method (EAM) potential [53], validated for Cu diffusion, grain boundary dynamics, and mechanical response. A three-dimensional particle model was constructed within a 450 × 450 × 900 $Å^3$ simulation domain (Fig. 4), comprising 11.1 million atoms with particle diameters of 2-6 nm, consistent with prior MD studies of NP sintering [43]. Atomic configurations, dislocation evolution, and crystallographic environments were analyzed using the Open Visualization Tool (OVITO) [54].

The sintering process was divided into three sequential stages. First, the system was heated to 523 K under a Nosé-Hoover thermostat to activate NP surface diffusion. Uniaxial compressive strains of 40% were then applied along the X- and Y-axes at a strain rate of 1×10^9 s^{-1}, mimicking experimental pressure-assisted sintering while maintaining zero lateral stress in non-loading directions. Finally, the system was equilibrated at 523 K for 100 ps to relax residual stresses induced by rapid deformation. This protocol replicated experimentally observed densification while balancing computational efficiency and physical accuracy.

Uniaxial compression simulations were conducted on sintered Cu NP configurations to investigate their mechanical response under conditions analogous to experimental loading. Prior to the compressive simulation, a relaxation process with variable box dimensions is performed to eliminate residual internal stresses. The compressive deformation is conducted under fully periodic boundary conditions using the NPT ensemble, maintaining a constant temperature of 300 K. A maximum compressive strain of 40% is applied, with a loading rate of 5×10^8 s^{-1}, to capture plasticity and failure behavior. To ensure uniaxial stress conditions representative of micromechanical testing, the lateral stress components were relaxed to zero throughout the simulations. This approach enables direct correlation between atomic-scale dislocation activity and the observed stress-strain responses, thereby bridging nanoscale mechanisms with macroscale mechanical performance.

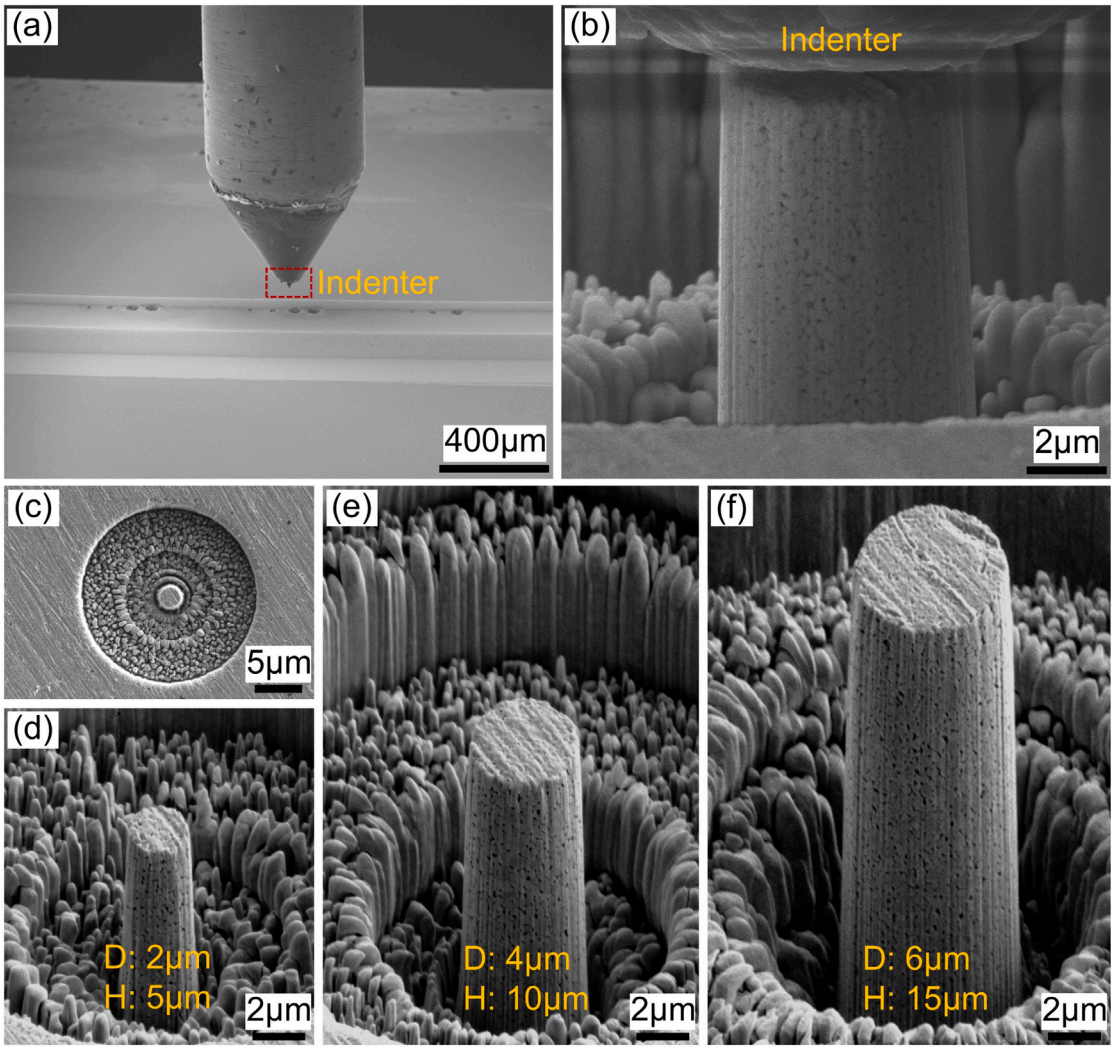

Fig. 2. SEM images of micro-pillars and compression setup: (a) Low-magnification view of the indenter approaching the sample surface; (b) high-magnification image showing the indenter in contact with a micro-pillar; (c) top-view of a micro-pillar; (d-f) micro-pillars with varying diameters and heights: (d) D = 2 μm, H = 5 μm; (e) D = 4 μm, H = 10 μm; (f) D = 6 μm, H = 15 μm.

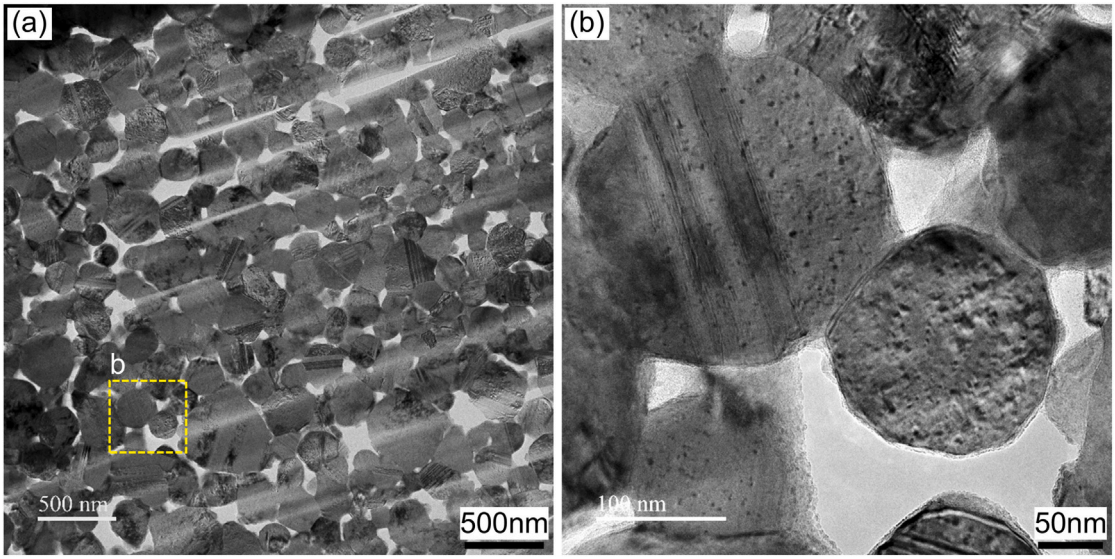

Fig. 3. TEM images of sintered Cu NPs: (a) Low-magnification overview showing the microstructure and particle distribution; (b) high-magnification image of the region marked in (a), highlighting particle interfaces and sintering necks.

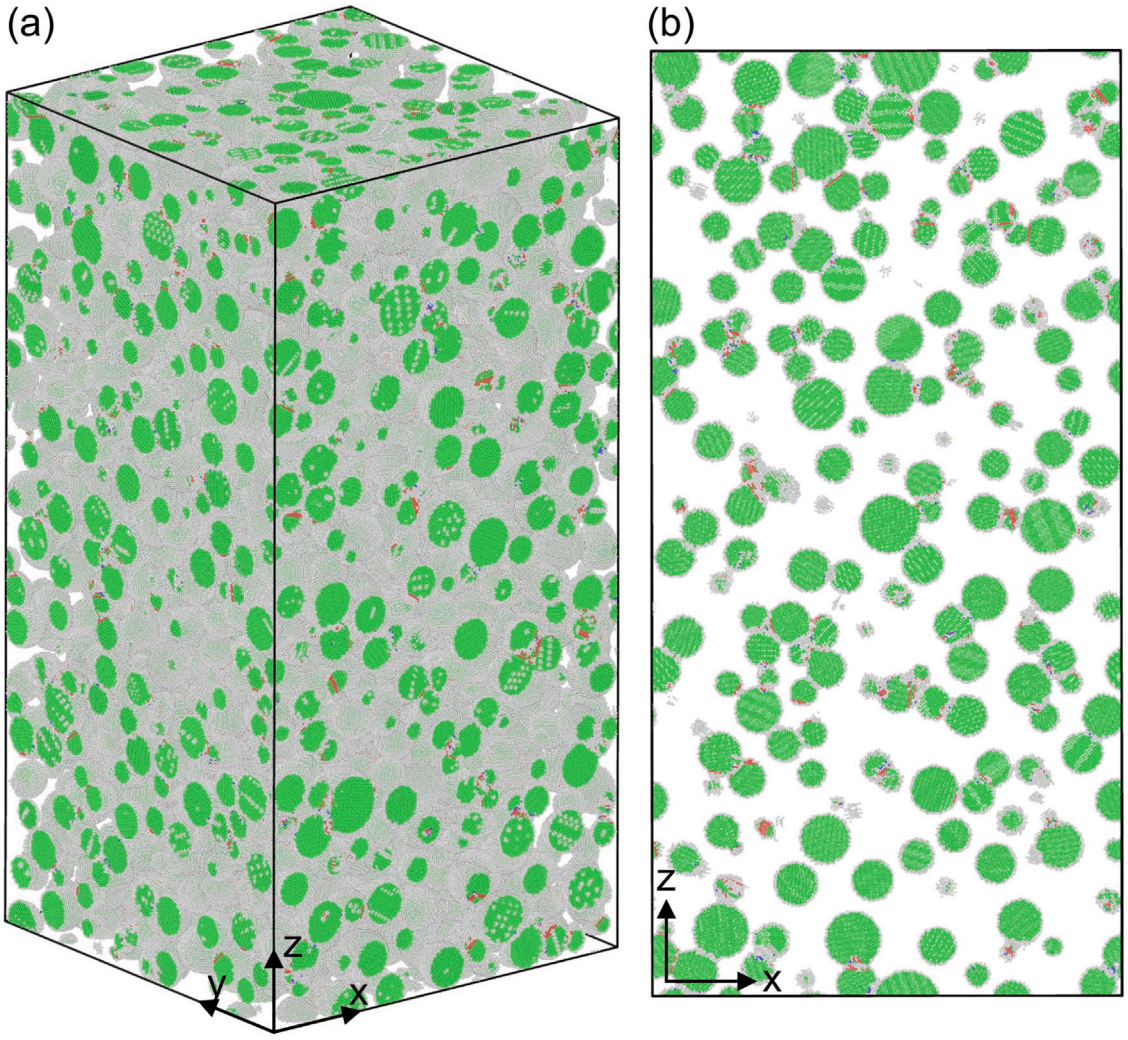

Fig. 4. Particle models for MD simulations: (a) Initial 3D configuration; (b) corresponding 2D cross-sectional view.

3. Results and discussion

3.1. Stress–strain curves

The mechanical properties of sintered Cu NP micro-pillars, as derived from micro-pillar compression (Figs. 5a–c) and nanoindentation tests (Fig. 6), exhibit distinct scaling trends across elastic and plastic regimes. The elastic modulus is defined as the slope of the elastic stage, while the yield strength is defined as the stress at 0.2% plastic strain [55]. While the elastic modulus remains stable across pillar diameters (29.5 ± 7.6 GPa to 33.9 ± 8.8 GPa), the yield strength decreases by 25.9% (812 ± 64 MPa at 2 μm to 643 ± 47 MPa at 6 μm). This divergence reflects the multiscale nature of deformation: elastic modulus, governed by atomic bonding and bulk porosity, demonstrates minimal size dependence, whereas yield strength is highly sensitive to microstructural heterogeneities (e.g., sintering necks, pore density) and dislocation dynamics. This characteristic size effect on yield strength in micro-pillar compression experiments has been reported extensively [19,24,25]. In smaller pillars (2 μm), the elevated surface-to-volume ratio promotes dislocation annihilation at free surfaces—a hallmark of the dislocation starvation mechanism observed in FCC metals [19]. However, the TEM-revealed microstructure, characterized by sintering necks and interparticle porosity, introduces competing effects. Sintering necks act as localized stress concentrators, governing dislocation nucleation and transmission between particles. Smaller pillars exhibit fewer necks per unit volume and reduced porosity due to shorter diffusion paths during sintering, resulting in stronger interfacial regions that resist dislocation-mediated plasticity. Conversely, larger pillars (6 μm) feature higher densities of sintering defects and pores (Fig. 5d), which diminish the effective load-bearing area and amplify stress localization, thereby reducing yield strength. Additionally, interparticle slip at weakened necks and pore clusters contributes to plasticity in larger pillars, creating a transition in dominant deformation modes from dislocation starvation in smaller pillars to porosity-driven weakening in larger ones.

The nanoindentation results (Fig. 6) further contextualize this behavior. The yield strength (670 ± 52 MPa) aligns closely with the 6 μm pillar data, suggesting that at the tens-of-micrometers scale probed by the spherical indenter (10 μm tip), deformation mechanisms resemble those in larger pillars, where porosity and weakened sintering necks dominate plasticity. Conversely, the elevated elastic modulus from nanoindentation (48.3 ± 11.1 GPa vs. 30 GPa in pillars) highlights the influence of testing methodology. Micro-pillar compression isolates the porous architecture, eliminating substrate constraints and providing a precise measurement of the intrinsic structure. In contrast, nanoindentation integrates contributions from both the porous network and the underlying bulk material, resulting in a higher apparent modulus.

3.2. Microstructure evolution during compression

The compressive deformation of sintered Cu NP micro-pillars exhibits pronounced size-dependent plasticity and strain localization, as

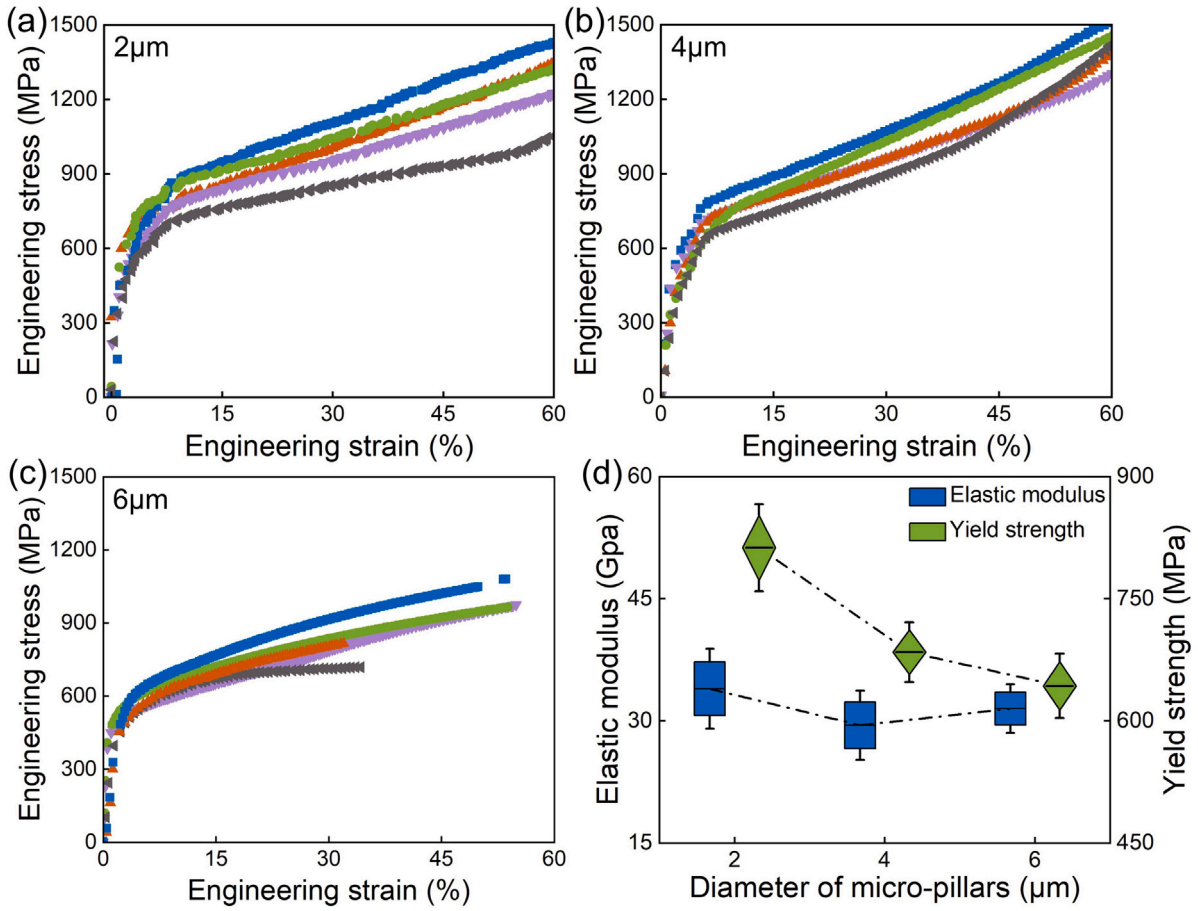

Fig. 5. Mechanical response of micro-pillars with varying diameters: (a–c) Engineering stress–strain curves for micro-pillars with diameters of 2 μm, 4 μm, and 6 μm, respectively; (d) summary of elastic modulus and yield stress as functions of pillar diameter.

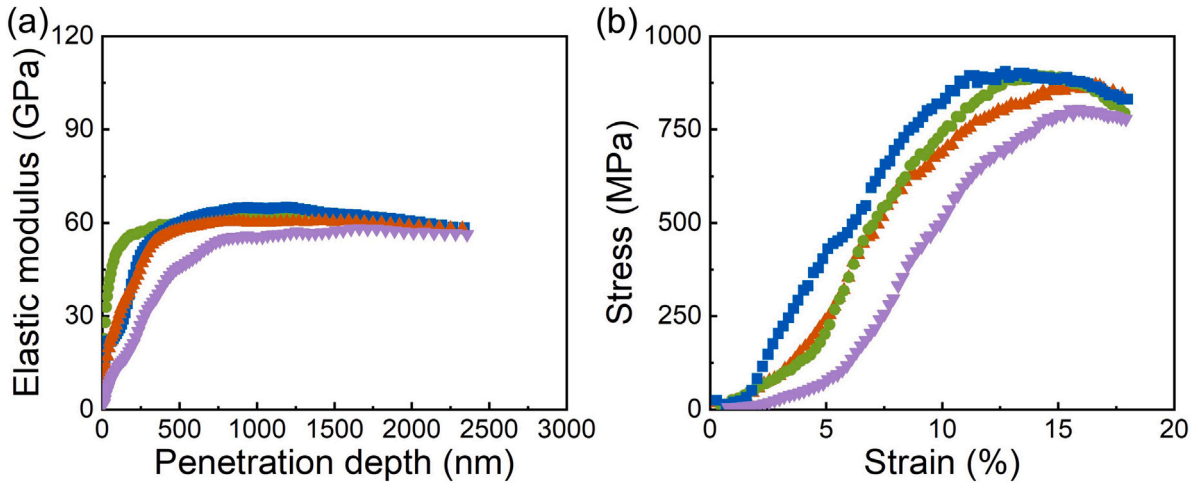

Fig. 6. Mechanical properties from nanoindentation tests: (a) Variation of elastic modulus with penetration depth during nanoindentation; (b) stress–strain curves.

revealed by SEM analysis (Fig. 7). Figs. 7a–c illustrate the evolution of a 6 μm pillar under increasing strains (0%, 15%, 30%), transitioning from an initially porous structure (Fig. 7a) to a laterally expanded morphology (Figs. 7b, c). This inflation, absent in bulk Cu where homogeneous dislocation glide ensures geometric stability [56], arises from the collapse of interparticle pores and non-uniform densification. Stress concentrations at interparticle necks promote preferential deformation, while the inherent porosity of sintered NPs redistributes strain heterogeneously, akin to deformation mechanisms in nanoporous metals [57]. Notably, smaller pillars (2 μm, Fig. 7d) collapse catastrophically into flattened cake-like morphologies, whereas larger pillars (6 μm, Fig. 7f retain structural integrity through distributed plasticity. The transition

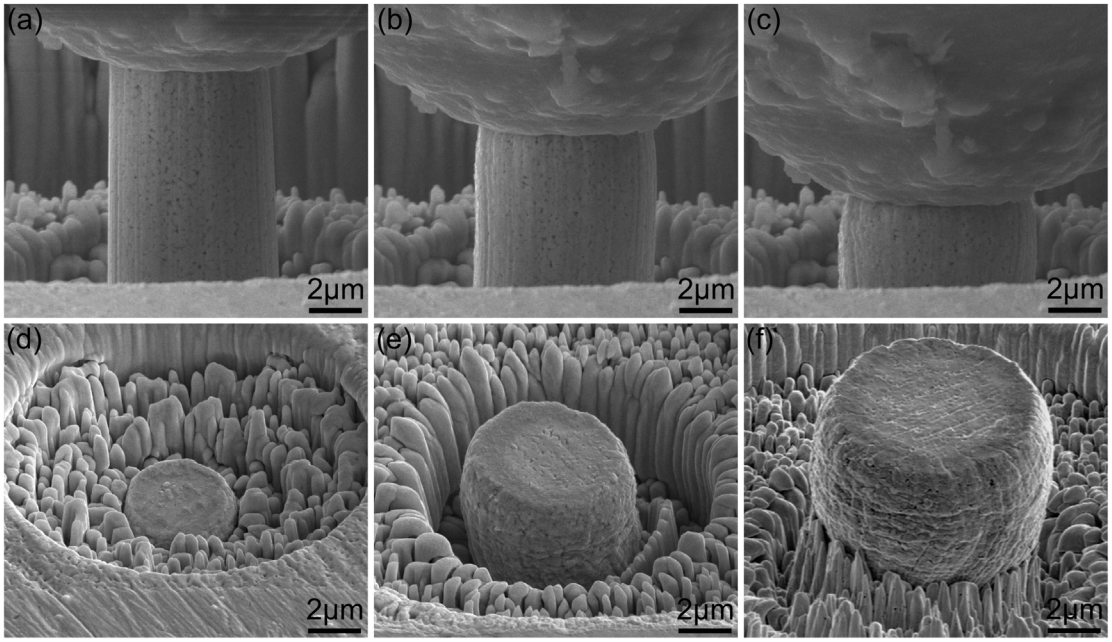

Fig. 7. SEM images of a micro-pillar under compression at increasing strains: (a) 0%, (b) 15%, and (c) 30%. (d–f) SEM images of compressed micro-pillars with diameters of 2 μm, 4 μm, and 6 μm, respectively.

from buckling-dominated failure (2 μm) to grain-boundary sliding (6 μm) mirrors behavior in nanocrystalline metals, where larger volumes accommodate strain via boundary-mediated processes [58].

TEM analysis of micro-pillars compressed to 25% and 50% strains (Fig. 8) further elucidates the microstructural origins of strain localization. At 25% strain (Figs. 8a, c–e), elongated grains in the midsection (Fig. 8d) contrast sharply with equiaxed grains in peripheral regions (Figs. 8c, e), reflecting heterogeneous dislocation activity. This strain partitioning resembles shear band formation in metallic glasses [59], though here driven by stress gradients between rigid NP cores and compliant interparticle boundaries. At 50% strain (Figs. 8b, f-h), severe grain flattening and porosity reduction in the midsection (Figs. 8f, g) coincide with retained equiaxed grains in adjacent zones (Fig. 8h), indicative of triaxial stress states activating Schmid-type slip systems [60]. The persistence of equiaxed grains in less-strained regions underscores the role of grain boundaries as barriers to dislocation motion, a phenomenon exacerbated in sintered NPs due to limited dislocation storage capacity. These observations parallel the hard core-soft shell model [61], yet with distinct dislocation dynamics governed by the interplay of porosity and grain boundary structure.

The deformation response is ultimately governed by the competition between dislocation-mediated plasticity, pore collapse, and sintering neck constraints. Porosity reduction at higher strains (Fig. 8b) suggests dislocation-driven densification. However, residual porosity in highly strained regions highlights kinetic limitations inherent to sintering-derived microstructures, where incomplete particle bonding restricts full densification. The heterogeneous strain distribution—localized slip at the midsection versus elastic accommodation at edges—diverges fundamentally from bulk Cu's homogeneous plasticity [62], instead resembling deformation in ultrafine-grained metals where boundary-mediated processes dominate [63]. The elongation of Cu NPs in strained zones (Figs. 8f, g) implies activation of multiple slip systems, while retained equiaxed grains (Fig. 8h) signify incomplete dislocation transmission across boundaries. This duality underscores how intrinsic defects (e.g., porosity, grain size gradients) amplify stress localization, bridging the gap between nanoparticle assemblies and bulk metals. To mitigate strain localization, optimizing sintering protocols to enhance interparticle bonding and minimize porosity could improve mechanical performance, offering critical insights for additive manufacturing of robust micro-architected metals.

3.3. TKD analysis

3.3.1. Grain structure analysis

The microstructural evolution of sintered Cu NP micro-pillars under uniaxial compression, as revealed by TKD in Fig. 9, demonstrates profound grain refinement. The initial microstructure (Fig. 9a) comprises a polycrystalline architecture with random grain orientations, reflecting the absence of preferential crystallographic alignment. Post-compression (Fig. 9b), dynamic recrystallization drives a 24.9% reduction in average grain size (250.4 nm to 187.9 nm) and a decrease in aspect ratio from 0.60 to 0.46, reflecting a transition to flattened, elongated grains. The observed grain refinement can be attributed to two synergistic mechanisms: dynamic recrystallization [64] and Hall–Petch strengthening [65]. Under high strain-rate deformation, dynamic recrystallization becomes particularly pronounced in nanocrystalline systems, where dislocation accumulation at grain boundaries triggers localized boundary reconstruction and nucleation of finer grains [66]. Concurrently, the reduced grain size activates the Hall–Petch mechanism [67,68], whereby increased grain boundary density strengthens the material by impeding dislocation motion. These coupled processes explain the significant strain hardening observed during compression.

Complementary analysis of geometrically necessary dislocation (GND) density (Fig. 10) elucidates the dislocation-mediated plasticity governing deformation. The GND density surges by 74.8%, from 1.15×10^{15} m^{-2} to 2.01×10^{15} m^{-2}. Spatial mapping (Figs. 10a, b) reveals preferential GND accumulation at grain boundaries and regions of severe plastic strain, consistent with Ashby's theory of non-uniform deformation in polycrystals [69]. The observed deformation behavior emerges from two interdependent micromechanical processes: First, lattice mismatch at grain boundaries creates localized stress fields that hinder dislocation glide, leading to characteristic dislocation pile-up configurations [70]. Second, the near-rigid body rotation of grains during plastic deformation magnifies these boundary misfit strains, requiring the coordinated generation of GNDs to maintain lattice continuity [71,72]. These mechanisms collectively promote a transition from conventional dislocation-mediated plasticity to grain boundary-dominated deformation, a phenomenon quantitatively analogous to that observed in nanotwinned Cu systems [73,74], where twin boundary constraints similarly alter the fundamental deformation pathways.

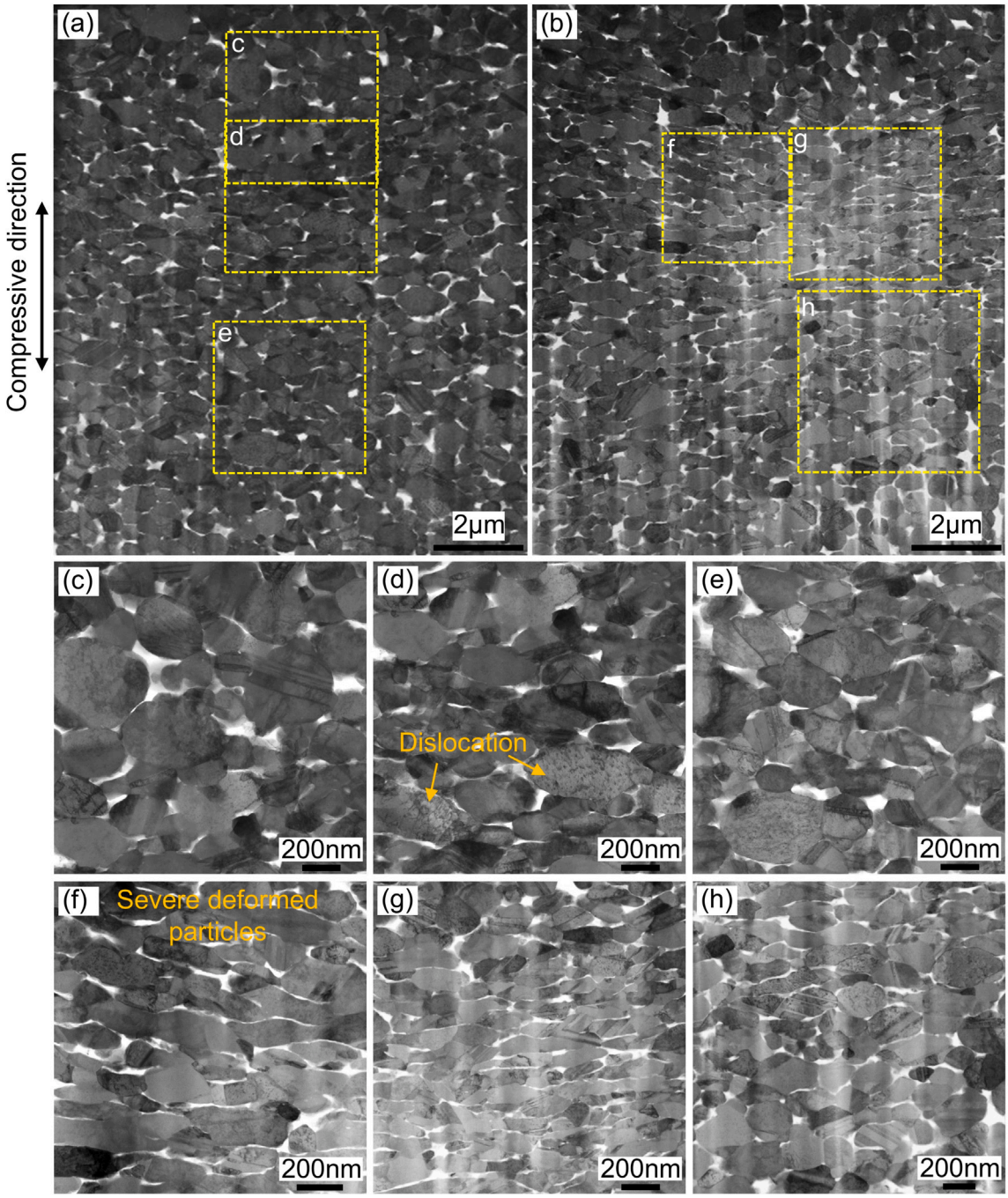

Fig. 8. Bright-field TEM images of micro-pillars at different strains: (a) 25% and (b) 50%. (c–e) Higher-magnification views of the region marked in (a); (f–h) corresponding magnified views of the region marked in (b).

The interplay between dynamic recrystallization and dislocation activity reveals a dual strengthening mechanism. First, grain refinement enhances boundary strengthening, as quantified by the Hall–Petch relationship modified for nanocrystalline systems [75–77]:

$$\sigma_y = \sigma_0 + kd^{-1/2} + \alpha Gb\sqrt{\rho_{\mathrm{GND}}} \quad (1)$$

Where d is the grain size and ρ_{GND} is the GND density. Second, the exponential rise in GND density facilitates dislocation strengthening through forest hardening, where tangled dislocations elevate the critical resolved shear stress [78]. The formation of dislocation forests (Fig. 10c) generates overlapping stress fields that further suppress slip, a behavior akin to deformation in ultrafine-grained alloys [79].

These findings highlight the competition between grain boundary-mediated processes and dislocation plasticity in sintered NPs. Unlike bulk Cu, where homogeneous dislocation multiplication ensures uniform strain [80], the limited dislocation storage capacity of NPs amplifies boundary-driven mechanisms. This underscores the necessity of optimizing sintering protocols to minimize porosity and enhance interparticle cohesion.

3.3.2. *Strain-induced anisotropic plasticity enhancement*

The mechanical response of sintered Cu NP micro-pillars under compression is governed by a complex interplay of grain rotation, dynamic recrystallization, and texture evolution, as revealed by orientation distribution function (ODF) analysis (Fig. 11) and Schmid

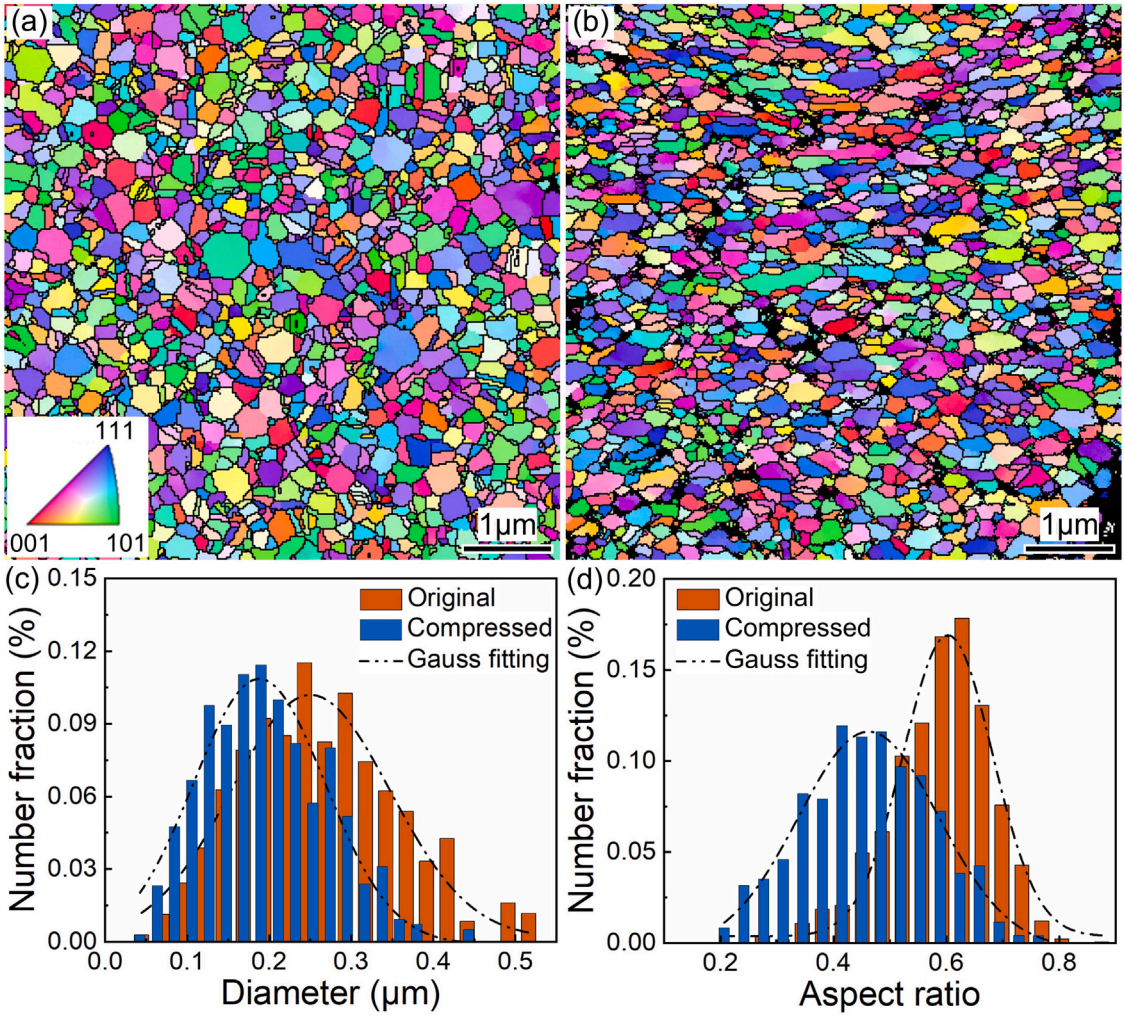

Fig. 9. Microstructural analysis of sintered Cu NP micro-pillars: (a, b) Inverse pole figure maps of longitudinal cross-sections in the original and compressed states; (c, d) statistical distributions of grain diameter and aspect ratio before and after compression, with Gaussian fitting.

factor mapping (Fig. 12). Utilizing Euler angles (ϕ_1, Φ, ϕ_2) in the Bunge convention to quantify crystallographic orientations [81], the ODF analysis demonstrates significant texture reorganization at 55% strain (Fig. 11). The as-sintered microstructure exhibits a near-random orientation distribution ($\phi_2 = 0°/45°/65°$ sections, max MRD = 2.143), with weak $S(\{123\}\langle 634\rangle)$, cubic ($\{100\}\langle 001\rangle$). Post-compression, however, pronounced Brass ($\{110\}\langle 112\rangle$) and S textures dominate (max MRD = 2.669), accompanied by emergent rotated cubic ($\{001\}\langle 110\rangle$), F, and R recrystallization textures. This transition arises from two synergistic mechanisms: (i) strain-induced grain rotation that amplifies boundary misfit strains, necessitating GND accumulation to maintain lattice continuity ($\rho_{GND} \uparrow 74.8\%$); (ii) dynamic recrystallization driven by adiabatic heating at high strain rates $> 10^{-3}$ s^{-1}, which promotes nucleation of strain-free grains with preferential orientations [82]. The persistence of heterogeneous porosity further localizes deformation, disrupting uniform grain rearrangement and amplifying texture heterogeneity—a behavior contrasting with fully dense nanocrystalline metals [83].

Schmid factor (m) analysis elucidates how these texture changes modulate slip system activity (Fig. 12). For face-centered cubic (FCC) Cu, where plasticity is mediated by $\{111\}\langle 110\rangle$ slip systems, the Schmid factor $m = \cos\phi\cos\lambda$ determines the resolved shear stress on slip planes [84]. In the pre-compressed state, the dominant S texture exhibits low m values (< 0.26) along the loading axis (Fig. 12a), corresponding to a hard orientation where limited slip system activation occurs. Post-compression, the emergence of rotated cubic texture enables four slip systems with $m = 0.41$ (Fig. 12b), creating a soft orientation that facilitates plasticity. This texture-mediated transition explains the 62% increase in the fraction of high-m grains ($0.42 < m < 0.5$) along the loading axis, while transverse directions show negligible changes (Figs. 12c, d). Such anisotropy aligns with the activation of duplex slip systems ($\{111\}\langle 110\rangle \times 2$) under uniaxial strain, where crystallographic reorientation reduces the critical resolved shear stress (τ_{CRSS}) by 34% (Table S2). The resultant strain hardening arises not from conventional dislocation accumulation but from texture-induced slip homogenization—a phenomenon distinct from bulk Cu's dislocation-dominated hardening [85].

The interdependence of texture evolution and mechanical behavior underscores the unique deformation physics in sintered NPs. Unlike coarse-grained metals where Hall–Petch strengthening dominates, the limited dislocation storage capacity of nanocrystalline Cu NPs shifts the deformation paradigm to grain boundary-mediated processes. The transition from S to rotated cubic texture (Fig. 11b) enhances boundary sliding compatibility, reducing stress concentrations at triple junctions [86]. Concurrently, GND accumulation at boundaries ($\rho_{GND} \approx 2.01 \times 10^{15}$ m^{-2}) generates back stresses that stabilize plastic flow, delaying shear band formation [87].

In conclusion, compression-induced texture evolution in sintered Cu NP micro-pillars orchestrates a dual strengthening-plasticization mechanism: (1) Recrystallization textures (rotated cubic/F/R) enhance slip system availability along the loading axis via high Schmid factor orientations ($m \geq 0.41$); (2) GND-mediated strain gradient plasticity stabilizes

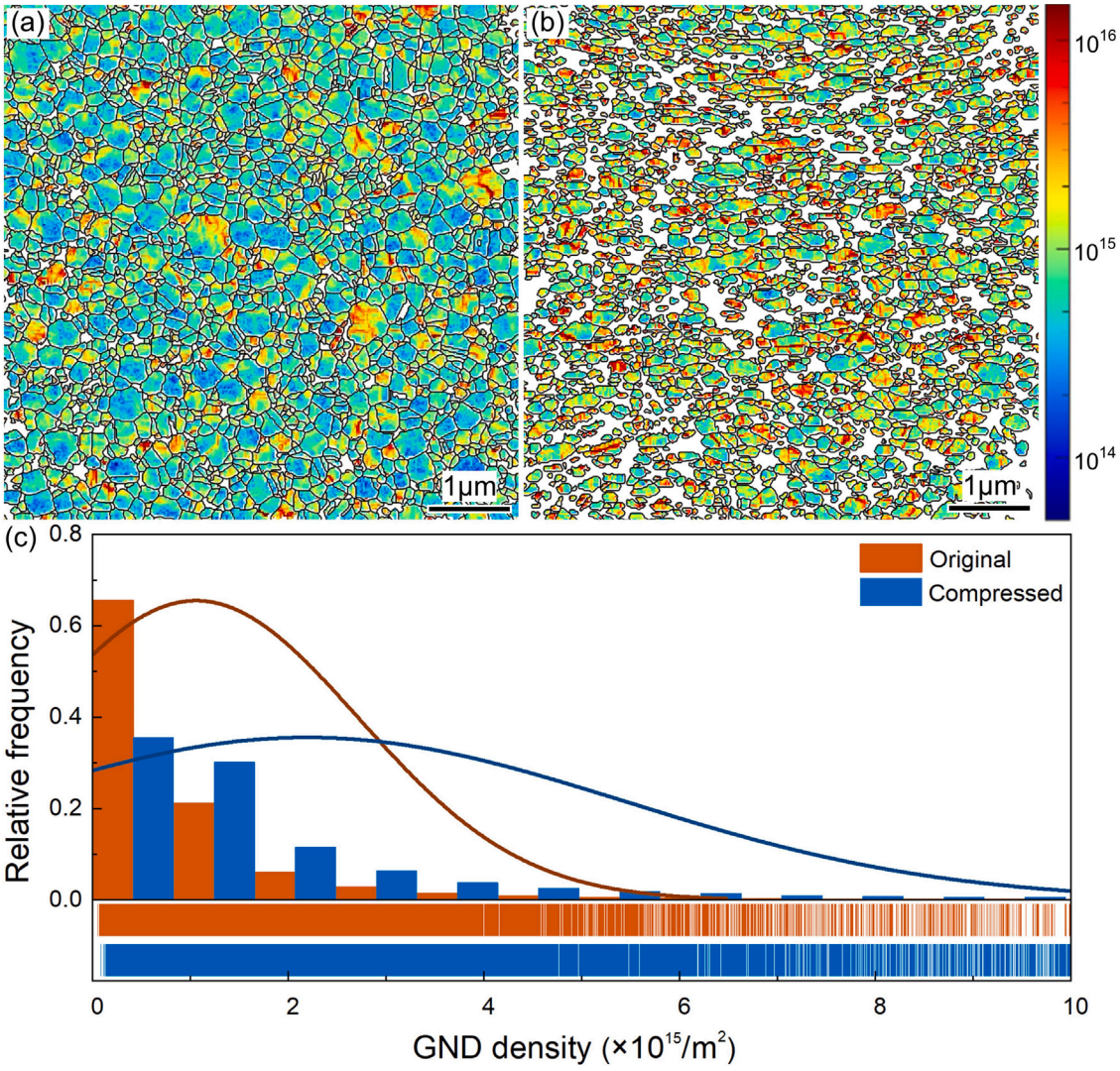

Fig. 10. GND analysis of Cu NP micro-pillars: (a) GND density map of the original microstructure; (b) GND density map after compression; (c) statistical distribution of GND density before and after deformation.

deformation through back stress hardening. This behavior, fundamentally distinct from both fully dense nanocrystalline and coarse-grained Cu, highlights the critical role of sintering-induced microstructural heterogeneity in tuning mechanical anisotropy. Future work should explore annealing protocols to mitigate porosity effects while preserving beneficial texture components.

3.4. Deformation mechanism by MD simulation

MD simulations illustrated in Fig. 13 reveal the evolution of sintering behavior in Cu NPs at different stages. Figs. 13a–c represent progressive sintering, with increasing degrees of particle coalescence and microstructural changes. Initially, in Fig. 13a, distinct particles are visible with minimal neck formation; the interparticle contact areas are limited, and porosity remains high. As the simulation advances to Fig. 13b, neck growth becomes more prominent, suggesting increased diffusion and atomic rearrangement at the particle interfaces. This leads to the gradual elimination of pores and densification of the structure. By stage shown in Fig. 13c, the sintered necks are significantly larger, and porosity is notably reduced, indicating advanced sintering and structural consolidation. Concurrently, dislocation evolution, denoted by red and blue features, intensifies from Fig. 13a–c. These dislocations originate primarily at the neck regions due to stress concentrations and atomic mismatch during particle bonding. The accumulation of dislocations in Fig. 13c suggests extensive plastic deformation and stress relaxation mechanisms active during sintering. This evolution highlights the complex interplay between diffusion-driven densification and defect generation in nanoscale systems. Such insight is critical for optimizing sintering parameters in nanoparticle-based manufacturing processes, ensuring desirable mechanical and structural properties in the final material.

Based on Fig. 14 and its correspondence to experimental observations in Fig. 8, the MD simulations reveal critical atomic-scale deformation mechanisms in sintered Cu NPs under compression. At 15% strain (Fig. 14c), initial particle rearrangement occurs with dislocation nucleation preferentially at sintering necks—consistent with experimental TEM observations of stress concentration at interparticle boundaries (Figs. 8c–e). These dislocations (visualized as line defects) facilitate early-stage plasticity through slip transmission between particles, mirroring the heterogeneous strain localization observed experimentally in pillar midsections. As strain increases to 30% (Fig. 14d), accelerated pore collapse and particle flattening dominate, with dislocations

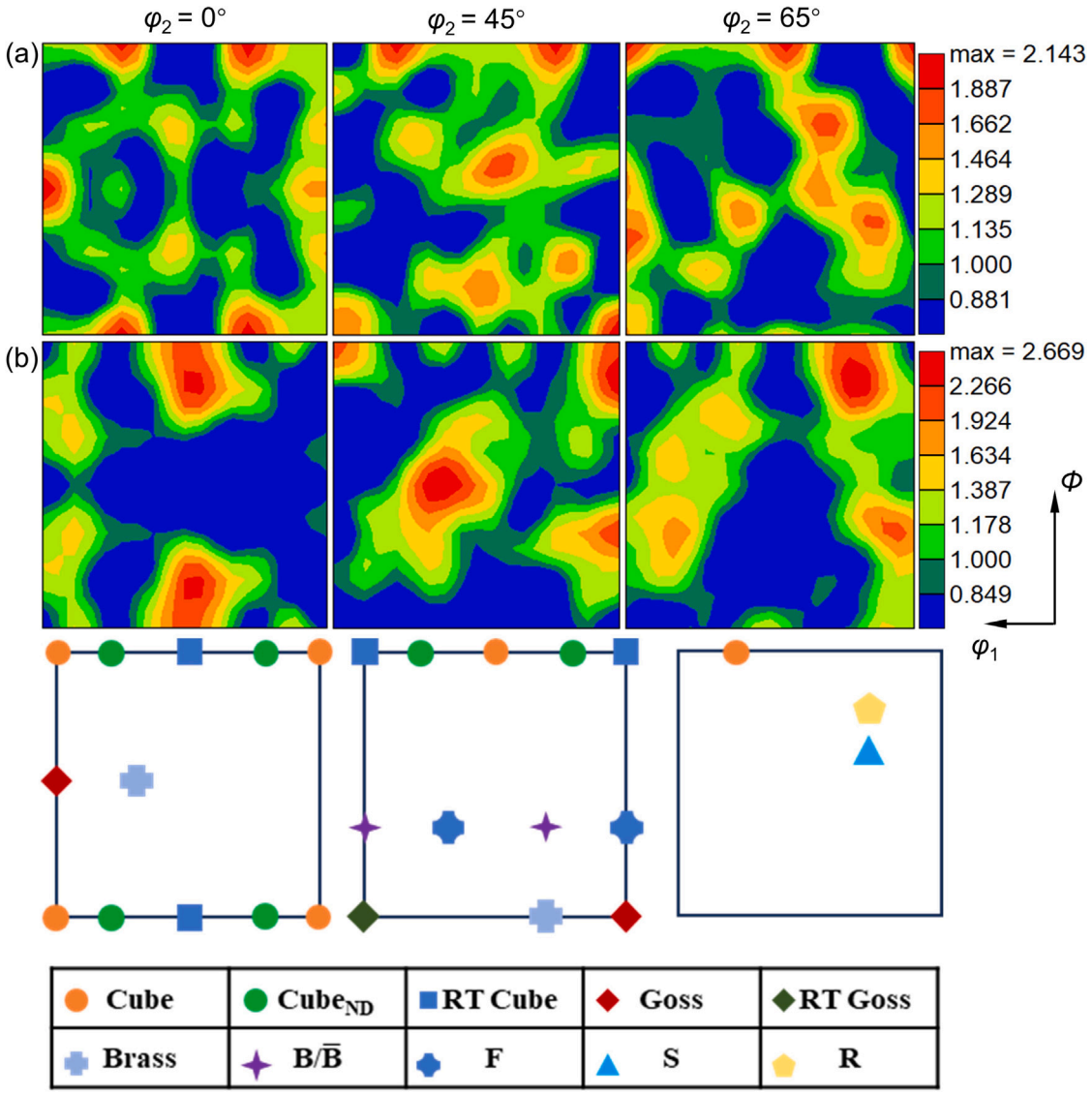

Fig. 11. Crystallographic texture evolution characterized by ODF sections at φ_2 = 0°, 45°, and 65°: (a) As-sintered microstructure showing random texture; (b) compressed microstructure revealing pronounced Brass {110}⟨112⟩ and S {123}⟨634⟩ components. Key texture components are annotated (Cube, Goss, Brass, etc.).

reorganizing into dense networks near grain boundaries. This aligns with experimental TEM evidence of severe grain flattening at 50% strain (Figs. 8f, g), where dislocation-mediated densification reduces porosity but leaves residual voids due to kinetic limitations in particle bonding.

The simulations further elucidate two key mechanisms implied by experimental data: First, the transition from distributed dislocation activity (15% strain) to localized shear patterning (30% strain) in Fig. 14d corresponds to the experimental transition from heterogeneous slip (Fig. 8a) to shear band-like features (Fig. 8b). Second, dislocation accumulation at triple junctions in Fig. 14d validates the experimentally measured 74.8% rise in GND density (Fig. 10), confirming how boundary misfit strains amplify back stresses. Critically, MD captures the atomic origins of hard coresoft shell behavior (Figs. 8c–h), showing dislocation pile-ups at rigid particle cores versus boundary sliding in compliant regions—bridging nanoscale mechanisms to microscale strain partitioning. These insights reinforce that optimizing sintering to minimize porosity and enhance neck cohesion (as simulated in pressure-assisted densification) could suppress strain localization, directly addressing the catastrophic failure observed in small pillars (Fig. 7d).

4. Conclusion

This study systematically investigated the mechanical behavior and deformation mechanisms of sintered Cu NP micro-pillars under compression, emphasizing the roles of size effects, grain evolution and dislocation dynamics. The findings offer a foundation for optimizing sintering processes and microstructural designs to enhance mechanical performance in microelectronic applications. The key findings are summarized as follows:

(1) Micro-pillar compression reveals a pronounced size effect, with yield strength decreasing by 25.9% (from 812 ± 64 MPa to 643 ± 47 MPa) as pillar diameter increases from 2 μm to 6 μm, attributed to dislocation starvation in smaller pillars and porosity-driven strain localization in larger pillars. Nanoindentation yields a higher elastic modulus (48.3 ± 11.1 GPa) than micropillar compression (29.5–33.9 GPa), reflecting substrate constraints in bulk-scale testing.

(2) SEM and TEM analyses identify a transition in deformation modes: smaller pillars (2 μm) exhibit catastrophic shear-driven collapse, while larger pillars (6 μm) retain structural integrity through distributed plasticity via grain boundary sliding. Heterogeneous strain localization arises from stress gradients between rigid nanoparticle cores

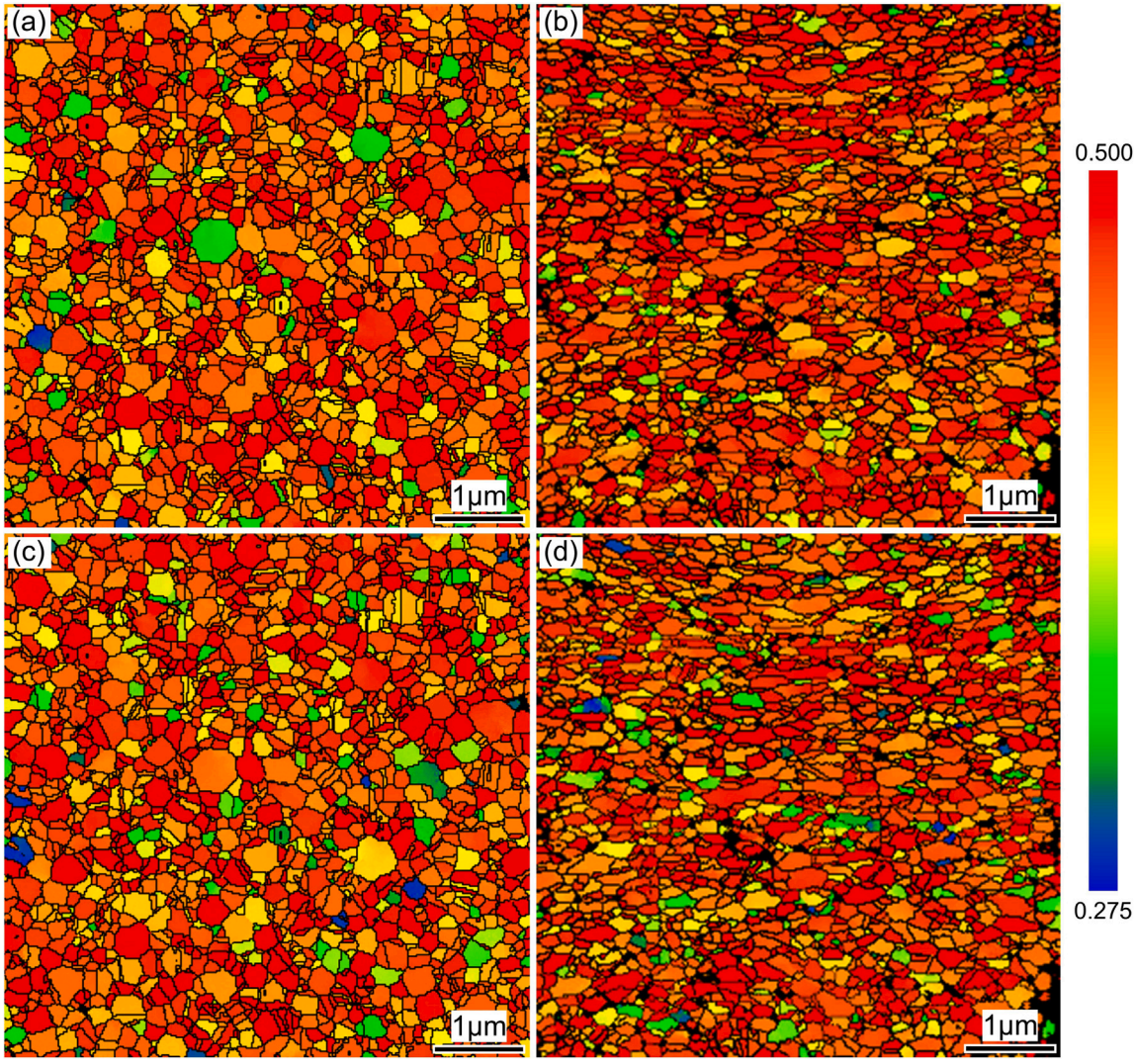

Fig. 12. Schmid factor maps: (a) pre-compression; (b) post-compression along loading axis; (c) pre- and (d) post-compression perpendicular to loading axis.

and compliant interparticle boundaries, with dislocation-mediated densification limited by residual porosity and incomplete sintering neck cohesion.

(3) TKD quantifies dynamic grain refinement (24.9% reduction in grain size) and a 74.8% escalation in GND density during compression. Texture evolves from random orientations to dominant Brass ($\{110\}\langle 112\rangle$) and $S(\{123\}\langle 634\rangle)$ components, coupled with a 62% increase in grains exhibiting high Schmid factors (> 0.42) along the loading axis, facilitating crystallographic slip homogenization and anisotropic plasticity.

(4) MD simulations elucidate atomic-scale deformation mechanisms, revealing preferential dislocation nucleation at sintering necks during initial compression (15% strain) and reorganization into dense networks near grain boundaries at higher strains (30%), which correlate with experimental observations of strain localization and GND density escalation.

CRediT authorship contribution statement

Xuyang Yan: Conceptualization, Investigation, Methodology, Software, Writing – original draft. **Leiming Du:** Methodology, Software, Supervision, Writing – review & editing. **Chao Gu:** Methodology, Software. **Tiancheng Tian:** Investigation, Methodology. **Chenshan Gao:** Investigation, Methodology. **Guoqi Zhang:** Supervision, Writing – review & editing. **Jiajie Fan:** Conceptualization, Supervision, Writing – review & editing.

Declaration of competing interest

The authors declare that they have no known competing financial interests or personal relationships that could have appeared to influence the work reported in this paper.

Acknowledgment

The work described in this paper was supported by the National Natural Science Foundation of China (Grant No. 52275559).

Appendix A. Supplementary data

Supplementary material related to this article can be found online at https://doi.org/10.1016/j.msea.2025.148684.

Data availability

Data will be made available on request.

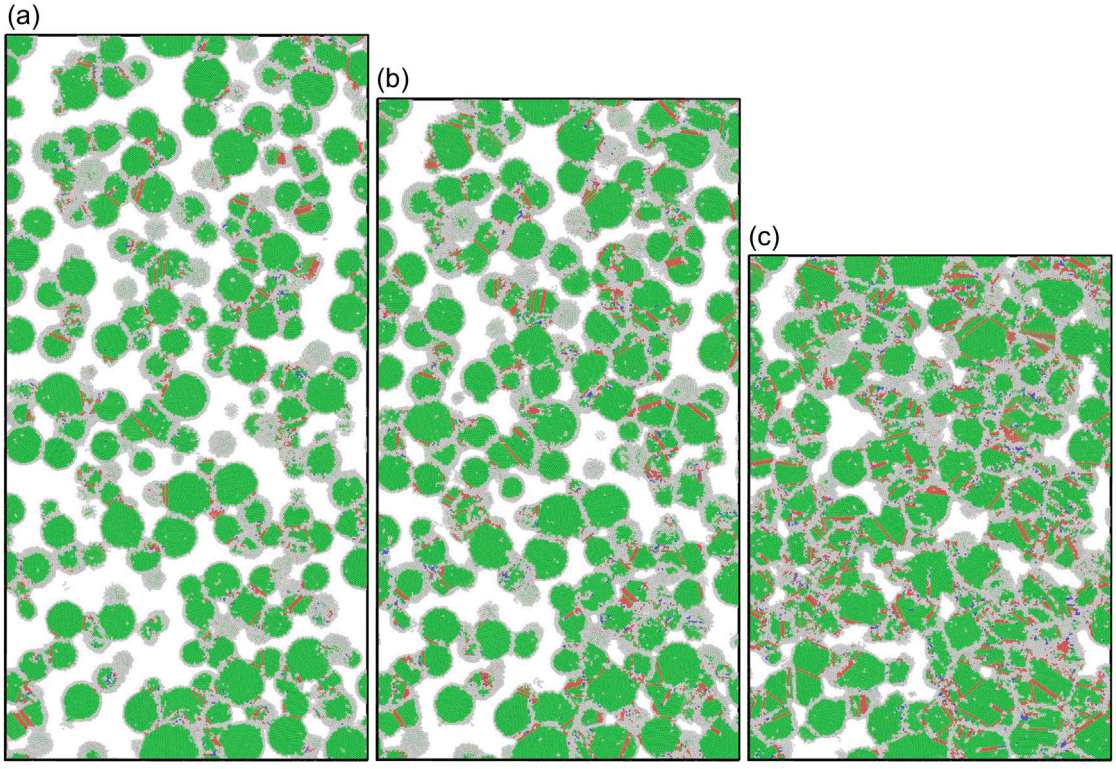

Fig. 13. Atomic-scale sintering process observed by MD simulation.

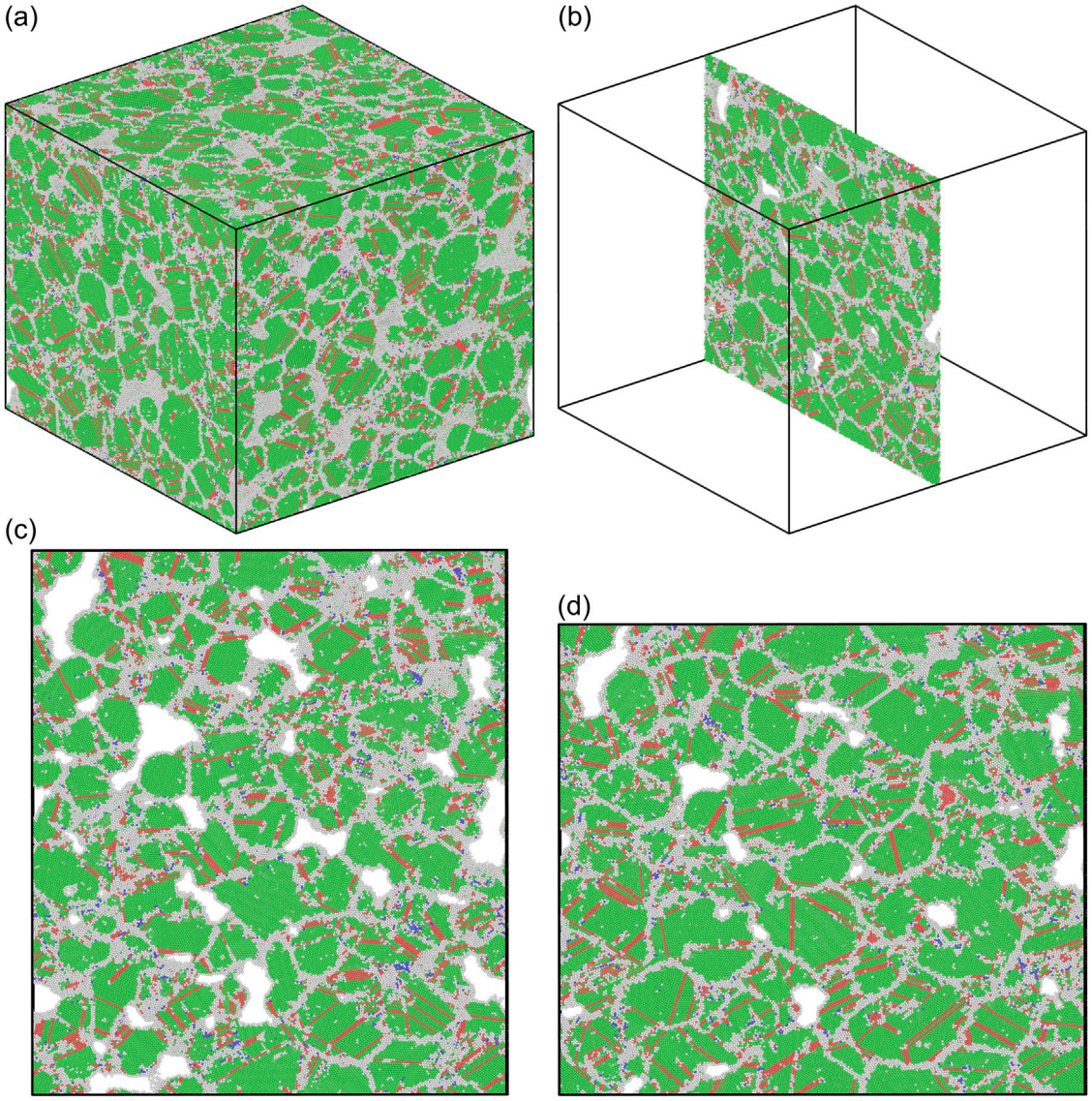

Fig. 14. (a) Compressived structure; (b) cross-section; (c) microstructure under 15% strain; (d) microstructure under 30% strain.

References

[1] H. Yan, Y.-H. Mei, X. Li, C. Ma, G.-Q. Lu, A multichip phase-leg IGBT module using nanosilver paste by pressureless sintering in formic acid atmosphere, IEEE Trans. Electron Devices 65 (10) (2018) 4499–4505.

[2] Z. Cui, Q. Jia, H. Zhang, Y. Wang, L. Ma, G. Zou, F. Guo, Review on shear strength and reliability of nanoparticle sintered joints for power electronics packaging, J. Electron. Mater. 53 (6) (2024) 2703–2726.

[3] K. Wakamoto, T. Namazu, Mechanical characterization of sintered silver materials for power device packaging: A review, Energies 17 (16) (2024) 4105.

[4] R. Riva, C. Buttay, B. Allard, P. Bevilacqua, Migration issues in sintered-silver die attaches operating at high temperature, Microelectron. Reliab. 53 (9–11) (2013) 1592–1596.

[5] Y. Tan, X. Li, X. Chen, Fatigue and dwell-fatigue behavior of nano-silver sintered lap-shear joint at elevated temperature, Microelectron. Reliab. 54 (3) (2014) 648–653.

[6] H. Zhang, W. Wang, H. Bai, G. Zou, L. Liu, P. Peng, W. Guo, Microstructural and mechanical evolution of silver sintering die attach for SiC power devices during high temperature applications, J. Alloys Compd. 774 (2019) 487–494.

[7] F. Le Henaff, S. Azzopardi, J.-Y. Delétage, E. Woirgard, S. Bontemps, J. Joguet, A preliminary study on the thermal and mechanical performances of sintered nano-scale silver die-attach technology depending on the substrate metallization, Microelectron. Reliab. 52 (9–10) (2012) 2321–2325.

[8] G. He, G. Hongcun, L. Shujin, Z. Junwen, Y. Yao, Compressive failure mechanism of sintered nano-silver, J. Mater. Res. 38 (18) (2023) 4201–4213.

[9] J. Ast, M. Göken, K. Durst, Size-dependent fracture toughness of tungsten, Acta Mater. 138 (2017) 198–211.

[10] R.H. Poelma, B. Morana, S. Vollebregt, E. Schlangen, H.W. van Zeijl, X. Fan, G.Q. Zhang, Tailoring the mechanical properties of high-aspect-ratio carbon nanotube arrays using amorphous silicon carbide coatings, Adv. Funct. Mater. 24 (36) (2014) 5737–5744.

[11] J. Yi, L. Wan, T. Shu, X. Zhang, F. Liu, G.J. Cheng, Unleashing multi-scale mechanical enhancement in NiTi shape memory alloy via annular intra-laser deposition with homogenized Ti2Ni nanoprecipitates, Acta Mater. 262 (2024) 119418.

[12] L.W. Yang, C. Mayer, N. Li, J. Baldwin, N.A. Mara, N. Chawla, J.M. Molina-Aldareguia, J. Llorca, Mechanical properties of metal-ceramic nanolaminates: Effect of constraint and temperature, Acta Mater. 142 (2018) 37–48.

[13] J. Stewart, L. Jiang, J. Williams, N. Chawla, Prediction of bulk tensile behavior of dual phase stainless steels using constituent behavior from micropillar compression experiments, Mater. Sci. Eng.: A 534 (2012) 220–227.

[14] S.Y. Ahn, Y. Wang, B. Vazic, R. Wheeler, P. Newell, Probing the mechanical performance of micro-architected porous structures through in situ characterization and analysis, JOM 75 (10) (2023) 4361–4375.

[15] J.M. Maita, S. Rommel, J.R. Davis, H. Ryou, J.A. Wollmershauser, E.P. Gorzkowski, B.N. Feigelson, M. Aindow, S.-W. Lee, Grain size effect on the mechanical properties of nanocrystalline magnesium aluminate spinel, Acta Mater. 251 (2023) 118881.

[16] C. Chen, K. Suganuma, Microstructure and mechanical properties of sintered Ag particles with flake and spherical shape from nano to micro size, Mater. Des. 162 (2019) 311–321.

[17] R. Ramachandramoorthy, S. Kalácska, G. Poras, J. Schwiedrzik, T.E. Edwards, X. Maeder, T. Merle, G. Ercolano, W.W. Koelmans, J. Michler, Anomalous high

strain rate compressive behavior of additively manufactured copper micropillars, Appl. Mater. Today 27 (2022) 101415.
[18] M. Zhang, X. Wang, A.D. Dupuy, J.M. Schoenung, X. Li, Study on strain rate–dependent deformation mechanism of WC–10 wt% Ni3Al cemented carbide by micropillar compression, Adv. Eng. Mater. 22 (3) (2020) 1900953.
[19] J.R. Greer, J.T.M. De Hosson, Plasticity in small-sized metallic systems: Intrinsic versus extrinsic size effect, Prog. Mater. Sci. 56 (6) (2011) 654–724.
[20] J. Wang, M. Ramajayam, E. Charrault, N. Stanford, Quantification of precipitate hardening of twin nucleation and growth in Mg and Mg-5Zn using micro-pillar compression, Acta Mater. 163 (2019) 68–77.
[21] L. Lu, T. Zhu, Y. Shen, M. Dao, K. Lu, S. Suresh, Stress relaxation and the structure size-dependence of plastic deformation in nanotwinned copper, Acta Mater. 57 (17) (2009) 5165–5173.
[22] W.S. Choi, B.C. De Cooman, S. Sandlöbes, D. Raabe, Size and orientation effects in partial dislocation-mediated deformation of twinning-induced plasticity steel micro-pillars, Acta Mater. 98 (2015) 391–404.
[23] J. Senger, D. Weygand, P. Gumbsch, O. Kraft, Discrete dislocation simulations of the plasticity of micro-pillars under uniaxial loading, Scr. Mater. 58 (7) (2008) 587–590.
[24] J.R. Greer, W.C. Oliver, W.D. Nix, Size dependence of mechanical properties of gold at the micron scale in the absence of strain gradients, Acta Mater. 53 (6) (2005) 1821–1830.
[25] Z. Shan, R.K. Mishra, S. Syed Asif, O.L. Warren, A.M. Minor, Mechanical annealing and source-limited deformation in submicrometre-diameter Ni crystals, Nat. Mater. 7 (2) (2008) 115–119.
[26] D. Jang, J.R. Greer, Size-induced weakening and grain boundary-assisted deformation in 60 nm grained Ni nanopillars, Scr. Mater. 64 (1) (2011) 77–80.
[27] Z. Guan, F.F. Le, J. Wu, J. Yang, R. Van Der Meulen, H. Chen, Influence of porosity on the mechanical properties of hybrid silver sintered joint, in: 2021 22nd International Conference on Electronic Packaging Technology, ICEPT, IEEE, 2021, pp. 1–5.
[28] V. Gaisina, M. Andersson, M. Bonvalet-Rolland, J. Odqvist, P.-L. Larsson, P. Gudmundson, On the mechanical behavior of sintered Astaloy-85Mo: Influence of porosity and sinter conditions, Mater. Sci. Eng.: A 841 (2022) 143052.
[29] M. Hamid, M.S. Saleh, A. Afrouzian, R. Panat, H.M. Zbib, Modeling of porosity and grain size effects on mechanical behavior of additively manufactured structures, Addit. Manuf. 38 (2021) 101833.
[30] W. Lv, J. Hu, J. Liu, C. Xiong, F. Zhu, Porosity effect on the mechanical properties of nano-silver solder, Nanotechnology 34 (16) (2023) 165701.
[31] X. Li, Y. Wei, W. Yang, H. Gao, Competing grain-boundary-and dislocation-mediated mechanisms in plastic strain recovery in nanocrystalline aluminum, Proc. Natl. Acad. Sci. 106 (38) (2009) 16108–16113.
[32] G. Vetterick, A. Leff, M. Marshall, J. Baldwin, A. Misra, K. Hattar, M. Taheri, Direct observation of a coincident dislocation-and grain boundary-mediated deformation in nanocrystalline iron, Mater. Sci. Eng.: A 709 (2018) 339–348.
[33] L. Du, K. Liu, D. Hu, O. Bäcke, X. Hu, X. Ji, J. Fan, R.H. Poelma, M.H. Colliander, G. Zhang, Microstructural and mechanical anisotropy in pressure-assisted sintered copper nanoparticles, Acta Mater. (2025) 120772.
[34] H. Fan, S. Aubry, A. Arsenlis, J.A. El-Awady, The role of twinning deformation on the hardening response of polycrystalline magnesium from discrete dislocation dynamics simulations, Acta Mater. 92 (2015) 126–139.
[35] M. Li, X. Tian, W. Jiang, Q. Wang, H. Fan, Mechanism of strain hardening of magnesium single-crystals: Discrete dislocation dynamics simulations, J. Mech. Phys. Solids 173 (2023) 105238.
[36] J. Li, Y. Li, T. Suo, Q. Wei, Numerical simulations of adiabatic shear localization in textured FCC metal based on crystal plasticity finite element method, Mater. Sci. Eng.: A 737 (2018) 348–363.
[37] J. Cheng, S. Ghosh, A crystal plasticity FE model for deformation with twin nucleation in magnesium alloys, Int. J. Plast. 67 (2015) 148–170.
[38] J. Hu, Z. Liu, K. Chen, Z. Zhuang, Investigations of shock-induced deformation and dislocation mechanism by a multiscale discrete dislocation plasticity model, Comput. Mater. Sci. 131 (2017) 78–85.
[39] V.K. Sahu, P. Chakraborty, M. Yadava, N.P. Gurao, Micro-mechanisms of anisotropic deformation in the presence of notch in commercially pure titanium: An in-situ study with CPFEM simulations, Int. J. Plast. 177 (2024) 103985.
[40] X. Long, K. Chong, Y. Su, L. Du, G. Zhang, Connecting the macroscopic and mesoscopic properties of sintered silver nanoparticles by crystal plasticity finite element method, Eng. Fract. Mech. 281 (2023) 109137.
[41] L. Ding, R.L. Davidchack, J. Pan, A molecular dynamics study of sintering between nanoparticles, Comput. Mater. Sci. 45 (2) (2009) 247–256.
[42] A. Malti, A. Kardani, A. Montazeri, An insight into the temperature-dependent sintering mechanisms of metal nanoparticles through MD-based microstructural analysis, Powder Technol. 386 (2021) 30–39.
[43] D. Hu, Z. Cui, J. Fan, X. Fan, G. Zhang, Thermal kinetic and mechanical behaviors of pressure-assisted Cu nanoparticles sintering: A molecular dynamics study, Results Phys. 19 (2020) 103486.
[44] G. Liu, H. Li, J. Cao, J. Shen, Effect of substrate surface roughness and parameters on the behavior of Cu nanoparticles sintering: A study by molecular dynamics simulation, Appl. Surf. Sci. 692 (2025) 162744.
[45] C. Kirchlechner, F. Toth, F.G. Rammerstorfer, F.D. Fischer, G. Dehm, Pre-and post-buckling behavior of bi-crystalline micropillars: Origin and consequences, Acta Mater. 124 (2017) 195–203.
[46] K. Vanstreels, C. Wu, M. Gonzalez, D. Schneider, D. Gidley, P. Verdonck, M.R. Baklanov, Effect of pore structure of nanometer scale porous films on the measured elastic modulus, Langmuir 29 (38) (2013) 12025–12035.
[47] A.J. Leide, R.I. Todd, D.E. Armstrong, Measurement of swelling-induced residual stress in ion implanted SiC, and its effect on micromechanical properties, Acta Mater. 196 (2020) 78–87.
[48] S. Huang, Q. Zhao, C. Lin, C. Wu, Y. Zhao, W. Jia, C. Mao, In-situ investigation of tensile behaviors of Ti–6Al alloy with extra low interstitial, Mater. Sci. Eng.: A 809 (2021) 140958.
[49] J. Ast, G. Mohanty, Y. Guo, J. Michler, X. Maeder, In situ micromechanical testing of tungsten micro-cantilevers using HR-EBSD for the assessment of deformation evolution, Mater. Des. 117 (2017) 265–266.
[50] A.A. Saleh, G. Casillas, E.V. Pereloma, K.R. Carpenter, C.R. Killmore, A.A. Gazder, A transmission kikuchi diffraction study of cementite in a quenched and tempered steel, Mater. Charact. 114 (2016) 146–150.
[51] B.M. Jenkins, J.O. Douglas, H.M. Gardner, D. Tweddle, A. Kareer, P.S. Karamched, N. Riddle, J.M. Hyde, P.A. Bagot, G.R. Odette, et al., A more holistic characterisation of internal interfaces in a variety of materials via complementary use of transmission kikuchi diffraction and atom probe tomography, Appl. Surf. Sci. 528 (2020) 147011.
[52] A.P. Thompson, H.M. Aktulga, R. Berger, D.S. Bolintineanu, W.M. Brown, P.S. Crozier, P.J. In't Veld, A. Kohlmeyer, S.G. Moore, T.D. Nguyen, et al., LAMMPS-a flexible simulation tool for particle-based materials modeling at the atomic, meso, and continuum scales, Comput. Phys. Comm. 271 (2022) 108171.
[53] Y. Mishin, M.J. Mehl, D.A. Papaconstantopoulos, A.F. Voter, J.D. Kress, Structural stability and lattice defects in copper: Ab initio, tight-binding, and embedded-atom calculations, Phys. Rev. B 63 (22) (2001) 224106.
[54] A. Stukowski, Visualization and analysis of atomistic simulation data with OVITO–the open visualization tool, Modelling Simul. Mater. Sci. Eng. 18 (1) (2009) 015012.
[55] D. Kramer, H. Huang, M. Kriese, J. Robach, J. Nelson, A. Wright, D. Bahr, W. Gerberich, Yield strength predictions from the plastic zone around nanocontacts, Acta Mater. 47 (1) (1998) 333–343.
[56] D. Xie, M.-J. Chen, J. Gigax, D. Luscher, J. Wang, A. Hunter, S. Fensin, M. Zikry, N. Li, A fundamental understanding of how dislocation densities affect strain hardening behavior in copper single crystalline micropillars, Mech. Mater. 184 (2023) 104731.
[57] H.-J. Jin, L. Kurmanaeva, J. Schmauch, H. Rösner, Y. Ivanisenko, J. Weissmüller, Deforming nanoporous metal: Role of lattice coherency, Acta Mater. 57 (9) (2009) 2665–2672.
[58] Q. Zhu, Q. Zhao, Q. Huang, Y. Chen, S. Suresh, W. Yang, Z. Zhang, H. Zhou, H. Gao, J. Wang, Grain boundary plasticity initiated by excess volume, Proc. Natl. Acad. Sci. 121 (12) (2024) e2400161121.
[59] A. Greer, Y. Cheng, E. Ma, Shear bands in metallic glasses, Mater. Sci. Eng.: R: Rep. 74 (4) (2013) 71–132.
[60] J. Paux, L. Morin, R. Brenner, D. Kondo, An approximate yield criterion for porous single crystals, Eur. J. Mech. A Solids 51 (2015) 1–10.
[61] S.S. Xie, O. Vasylkiv, V. Silberschmidt, A.I. Tok, Bio-inspired structured boron carbide-boron nitride composite by reactive spark plasma sintering: This paper describes the prototyping of an approach to improve mechanical properties of conventional composites, mimicking biological material structured 'hard'core and 'soft'matrix system to efficiently transfer load stress, dissipate energy and resist cracking, by reactive spark plasma sintering (SPS) of boron carbide B4C carried out in a nitrogen N2 gas environment, Virtual Phys. Prototyp. 8 (4) (2013) 253–258.
[62] B. Hansen, J. Carpenter, S. Sintay, C. Bronkhorst, R. McCabe, J. Mayeur, H. Mourad, I. Beyerlein, N. Mara, S. Chen, et al., Modeling the texture evolution of Cu/Nb layered composites during rolling, Int. J. Plast. 49 (2013) 71–84.
[63] J. Zhang, G. Liu, J. Sun, Comparisons between homogeneous boundaries and heterophase interfaces in plastic deformation: Nanostructured Cu micropillars vs. nanolayered Cu-based micropillars, Acta Mater. 61 (18) (2013) 6868–6881.
[64] J. Zimmerman, E. Rabkin, Nanoparticle recrystallization: kinetics and size-dependent behavior, Acta Mater. 292 (2025) 121028.
[65] N. Hansen, Hall–Petch relation and boundary strengthening, Scr. Mater. 51 (8) (2004) 801–806.
[66] H. Toda, T. Kamiko, Y. Tanabe, M. Kobayashi, D. Leclere, K. Uesugi, A. Takeuchi, K. Hirayama, Diffraction-amalgamated grain boundary tracking for mapping 3D crystallographic orientation and strain fields during plastic deformation, Acta Mater. 107 (2016) 310–324.
[67] S. Takeuchi, The mechanism of the inverse Hall–Petch relation of nanocrystals, Scr. Mater. 44 (8–9) (2001) 1483–1487.
[68] R.B. Figueiredo, M. Kawasaki, T.G. Langdon, Seventy years of Hall–Petch, ninety years of superplasticity and a generalized approach to the effect of grain size on flow stress, Prog. Mater. Sci. 137 (2023) 101131.

[69] M. Ashby, The deformation of plastically non-homogeneous materials, Philos. Mag.: A J. Theor. Exp. Appl. Phys. 21 (170) (1970) 399–424.
[70] L.M. Brown, Dislocation pile-ups, slip-bands, ellipsoids, and cracks, Mater. Sci. Eng.: A 400 (2005) 2–6.
[71] M. Calcagnotto, D. Ponge, E. Demir, D. Raabe, Orientation gradients and geometrically necessary dislocations in ultrafine grained dual-phase steels studied by 2D and 3D EBSD, Mater. Sci. Eng.: A 527 (10–11) (2010) 2738–2746.
[72] L. Toth, C. Gu, B. Beausir, J.J. Fundenberger, M. Hoffman, Geometrically necessary dislocations favor the Taylor uniform deformation mode in ultra-fine-grained polycrystals, Acta Mater. 117 (2016) 35–42.
[73] Y.M. Wang, F. Sansoz, T. LaGrange, R.T. Ott, J. Marian, T.W. Barbee Jr., A.V. Hamza, Defective twin boundaries in nanotwinned metals, Nat. Mater. 12 (8) (2013) 697–702.
[74] J. Zhao, J. Zhang, L. Cao, Y. Wang, P. Zhang, K. Wu, G. Liu, J. Sun, Zr alloying effect on the microstructure evolution and plastic deformation of nanostructured Cu thin films, Acta Mater. 132 (2017) 550–564.
[75] E.N. Hahn, M.A. Meyers, Grain-size dependent mechanical behavior of nanocrystalline metals, Mater. Sci. Eng.: A 646 (2015) 101–134.
[76] C.S. Pande, B. Rath, M. Imam, Effect of annealing twins on Hall–Petch relation in polycrystalline materials, Mater. Sci. Eng.: A 367 (1–2) (2004) 171–175.
[77] C.S. Pande, R.A. Masumura, Grain growth and deformation in nanocrystalline materials, Mater. Sci. Eng.: A 409 (1–2) (2005) 125–130.
[78] S. Rao, C. Woodward, B. Akdim, E. Antillon, T. Parthasarathy, J. El-Awady, D. Dimiduk, Large-scale dislocation dynamics simulations of strain hardening of Ni microcrystals under tensile loading, Acta Mater. 164 (2019) 171–183.
[79] H. Lanjewar, S. Naghdy, F. Vercruysse, L.A. Kestens, P. Verleysen, Severe plastically deformed commercially pure aluminum: Substructure, micro-texture and associated mechanical response during uniaxial tension, Mater. Sci. Eng.: A 764 (2019) 138195.
[80] A.T. Jennings, J. Li, J.R. Greer, Emergence of strain-rate sensitivity in Cu nanopillars: Transition from dislocation multiplication to dislocation nucleation, Acta Mater. 59 (14) (2011) 5627–5637.
[81] T. Britton, J. Jiang, Y. Guo, A. Vilalta-Clemente, D. Wallis, L. Hansen, A. Winkelmann, A. Wilkinson, Tutorial: Crystal orientations and EBSD—Or which way is up? Mater. Charact. 117 (2016) 113–126.
[82] T. Al-Samman, G. Gottstein, Dynamic recrystallization during high temperature deformation of magnesium, Mater. Sci. Eng.: A 490 (1–2) (2008) 411–420.
[83] X. Li, L. Lu, J. Li, X. Zhang, H. Gao, Mechanical properties and deformation mechanisms of gradient nanostructured metals and alloys, Nat. Rev. Mater. 5 (9) (2020) 706–723.
[84] W. Zhang, Y. Gao, Y. Xia, H. Bei, Indentation Schmid factor and incipient plasticity by nanoindentation pop-in tests in hexagonal close-packed single crystals, Acta Mater. 134 (2017) 53–65.
[85] C. Li, K. Yang, Y. Gao, L. Wang, Dislocation-dominated void nucleation in shock-spalled single crystal copper: mechanism and anisotropy, Int. J. Plast. 155 (2022) 103331.
[86] R.R. Eleti, A.H. Chokshi, A. Shibata, N. Tsuji, Unique high-temperature deformation dominated by grain boundary sliding in heterogeneous necklace structure formed by dynamic recrystallization in HfNbTaTiZr BCC refractory high entropy alloy, Acta Mater. 183 (2020) 64–77.
[87] B. Poole, F.P. Dunne, Slip band interactions and GND latent hardening in a galling resistant stainless steel, Mater. Sci. Eng.: A 813 (2021) 141176.